



Enhancing catalytic activity of zeolitic octahedral metal oxides through zinc incorporation for ethane oxidative dehydrogenation

Bolun Yu^a, Denan Li^a, Qianqian Zhu^{a,*}, Shufan Yao^a, Lifeng Zhang^b, Yanshuo Li^{a,*}, Zhenxin Zhang^{a,*}

^a School of Materials Science and Chemical Engineering, Ningbo University, Ningbo 315211, China

^b Zhejiang Hymater New Materials Co., Ltd. Ningbo, Zhejiang 315034, China



ARTICLE INFO

Keywords:

Zeolitic octahedral metal oxide
Oxidative dehydrogenation
Ethane to ethylene
Microporous
Zinc

ABSTRACT

Zeolitic octahedral metal oxides possess both redox properties and microporosity, making them highly active for catalysis. Tuning the property of micropore by incorporating transition metal ion in the pore improves the catalytic activity greatly. In this study, single Zn species was incorporated into a micropore of a zeolitic octahedral metal oxide based on vanadomolybdate. Structural characterization demonstrated that the crystalline structure remained unchanged, and the micropores remained unblocked in the presence of Zn. Furthermore, this incorporation of Zn improved the catalytic activity of ethane oxidative dehydrogenation, achieving a 50 % of ethane conversion and 90% of selectivity. The yield of ethylene remained consistently at 45 % over 35 h, demonstrating the high stability of the catalyst. Mechanism study revealed that the isolated Zn site not only activated both O₂ and ethane, but also stabilized intermediates and transition states, leading to an increase in catalyst activity.

1. Introduction

Ethylene (C₂H₄) stands as a pivotal raw chemical compound with numerous applications in the manufacture of polymers, rubber, fiber, vinyl chloride, styrene, and other high-value products [1,2]. Ethane (C₂H₆) resides as one of the most prevalent constituents of natural gas and shale gas, exerting a strong greenhouse effect [3–5]. Direct emission of C₂H₆ into the atmosphere precipitates air pollution and contributes to global warming. The conversion of C₂H₆ to C₂H₄ turns this waste compound into a valuable chemical. The catalytic dehydrogenation of C₂H₆ to C₂H₄ offers several advantages over conventional C₂H₆ steam cracking, including reduced energy consumption and lower greenhouse gas emissions [6–8]. There are two pathways for the catalytic dehydrogenation of C₂H₆ into C₂H₄: non-oxidative dehydrogenation and oxidative dehydrogenation (ODH) [9,10]. Research has highlighted the advantages of C₂H₆ ODH, such as its spontaneous process in thermodynamics, exothermic nature of reaction, and low temperature requirement.

Numerous catalysts have undergone development for C₂H₆ ODH over the past few decades, mainly divided into two categories: molecular sieve supported catalysts and mixed metal oxides catalysts [5,11–13].

There are three types for mixed metal oxides catalysts: (i) noble metal containing catalysts [14,15]; (ii) non-reducible mixed oxides, including rare earth oxide-based catalysts [9,16–19], halide doped perovskites [20], alkali and alkaline-earth containing oxides [21]; (iii) reducible mixed metal oxides catalysts, including V and Mo-based mixed oxides [22], P and V-based oxides [23], Ni-based oxides [24–26], Cr-based oxides [19], and Co-based oxides [18,26–29]. However, it is essential to note that non-reducible mixed oxides, noble metal-containing catalysts, and molecular sieve supported catalysts do exhibit certain limitations such as high reaction temperature, high energy consumption, and low activity [13,30]. As a result, the ongoing research in ODH catalysts increasingly focuses on the development of catalysts with redox properties.

MoVTeNb oxide is a particularly intriguing catalyst among those reported catalysts with redox properties for C₂H₆ ODH [31–35]. Studies have demonstrated that this catalyst exhibits high C₂H₆ conversion with good C₂H₄ selectivity at 420 °C. The previous researcher has confirmed that the active site for C₂H₆ ODH is located in the heptagonal channel. However, the heptagonal channel is obstructed due to partial occupation by transition metal ions, necessitating the relatively elevated reaction temperature [36,37].

* Corresponding authors.

E-mail addresses: zhuqianqian@nbu.edu.cn (Q. Zhu), liyanshuo@nbu.edu.cn (Y. Li), zhangzhenxin@nbu.edu.cn (Z. Zhang).

In contrast, Zeolitic vanadomolybdate (VM) catalyst successfully addresses this issue. The framework of VM is composed of pentagon units of $(\text{Mo}_6\text{O}_{21})$ linked together by MO_6 ($\text{M} = \text{Mo}$ or V), leading to a structural composition mainly composed of metal-oxygen octahedra - known as zeolitic octahedral metal oxides (ZOMOs) [38,39]. Notably, VM shares an isomorphic relationship with MoVTeNb oxide, but in the case of VM, the pore blocking ions are removed, and the micropores are entirely open. This pivotal distinction leads to a high catalytic activity for VM, accompanied by a significantly reduced reaction temperature when compared to MoVTeNb oxide [40]. Moreover, VM exhibits high structural and elemental diversity, with variations in properties and application performance attributed to its structure and chemical composition. By tuning the microenvironment of the heptagonal channel within VM, it becomes possible to achieve a substantial enhancement in catalytic activity [41].

In this work, we present the synthesis of a zinc vanadomolybdate-based ZOMO, denoted as ZVM, where the heptagonal channel of VM was tuned by incorporating isolated Zn ions. Structural analysis confirmed that Zn incorporation did not change the crystalline structure of the material; Zn occupied the wall of the heptagonal channel without blocking it. ZVM catalyzed the ODH of C_2H_6 with high selectivity towards C_2H_4 as the major product, even at low temperatures. Additionally, ZVM exhibited superior catalytic activity compared to VM. The stable nature of ZVM enabled long-term stability for C_2H_6 ODH. The isolated Zn site activated O_2 and C_2H_6 while stabilizing intermediates and transition states, thereby contributing to the enhanced catalytic activity.

2. Experimental

2.1. Synthesis of Zn incorporated VM by a hydrothermal method

The synthesis of the catalyst was shown in [Scheme S1](#).

2.1.1. Synthesis of $(\text{CH}_3\text{NH}_3)_6\text{Mo}_7\text{O}_{24}$ (MAHM)

$(\text{CH}_3\text{NH}_3)_6\text{Mo}_7\text{O}_{24}$ (MAHM) was prepared by previously reported method [34]. First, 21.594 g of MoO_3 (0.150 mol, 99.5 %, Aladdin) was dissolved in 33.2 mL of 25 %– 30 % methylamine solution (methylamine: 0.210–0.251 mol, General-reagent). After MoO_3 being completely dissolved, the solution was evaporated under vacuum ($p/p_0 = 0.03$) at 75 °C, then a solid powder was obtained. The powder was dried in air at 80 °C overnight, and 26 g of MAHM was obtained.

2.1.2. Synthesis of ZVM

First, MAHM (8.020 g, 4.42 mmol) were dissolved in 135 mL of water (Millipore grade) at 30 °C stirred for 10 min. Meanwhile VOSO_4 (2.650 g, 99 %, 13.97 mmol) were dissolved in 45 mL of water (Millipore grade) at 30 °C and stirred for 10 min. Mixing the two aqueous solutions at 30 °C and stirred for 30 min. $\text{ZnSO}_4 \cdot 7 \text{ H}_2\text{O}$ (0.805 g, 99 %, 2.8 mmol) were added to the mixture and stirred for 30 min. The pH of mixture was 2.8 and then removing the residual oxygen by N_2 bubbling (100 mL/min) for 10 min. Then, the mixture was added into an autoclave with a 200 mL Teflon inner vessel with a thin Teflon sheet of 2000 cm^2 , and the autoclave was heated at 175 °C for 48 h in an oven. The crude solid (about 4.2 g) was isolated from the reaction mixture by filtration, washed with 1000 mL of water, and dried at 80 °C overnight.

2.1.3. Purification of the catalyst

Adding 105 mL of an aqueous solution of oxalic acid (0.4 mol/L) into the crude solid, which was stirred at 60 °C for 30 min, followed by washing with 1000 mL of water (Millipore grade). The sample after the purification is abbreviated as ZVM, and the yield was 2.0 g. Elemental analysis for $\text{Zn}_{1.1}[\text{Mo}_{30}\text{V}_{10}\text{O}_{112.8}] \cdot 9 \text{ H}_2\text{O}$, calc: Zn 1.49; Mo, 53.13; V, 9.46. found: Zn, 1.32; Mo, 53.06; V, 9.39.

2.1.4. Catalysts with different V and Zn content

The catalysts with various Zn contents were prepared following the same procedure only with different $\text{ZnSO}_4 \cdot 7 \text{ H}_2\text{O}$ content in precursor solution. The catalysts are abbreviated as ZVM-XZn where X indicates molar ratio of Zn to V in precursor solution.

The catalysts with various V contents were prepared following the same procedure only with different $\text{VOSO}_4 \cdot 7 \text{ H}_2\text{O}$ content in precursor solution. The catalysts are abbreviated as ZVM-XV where X indicates molar ratio of V to Mo in precursor solution.

2.1.5. Heat-treatment of the catalyst

ZVM was calcined in air, N_2 , and C_2H_6 for 2 h with a heating ramp of 10 °C/min, which was abbreviated as ZVM-AX, ZVM-NX, and ZVM-EX, where X = calcination temperature. Hydrogen calcination of ZVM was carried out under Hydrogen for 2 h which abbreviated as ZVM-HX, where X = calcination temperature. ZVM after calcinating sequentially air and C_2H_6 for 2 h was abbreviated as ZVM-AEX (X = calcination temperature).

2.2. Synthesis of Zn incorporated VM by an impregnation method

Zn supported VM was synthesized by impregnation method. $(\text{CH}_3\text{COO})_2\text{Zn}$ (0.183 g, 99 %, 1 mmol based on Zn) dissolved in distilled water (10 mL) was mixed with VM (2.360 g, 15 mmol based on Mo). The impregnation was performed and stirred for 6 h at room temperature. Then, the materials were dried at 80 °C overnight and calcined in air at 400 °C for 2 h. The material after calcination was abbreviated as Zn-VM; the yield was 2.5 g.

2.3. In situ IR measurements

In situ Diffuse Reflectance Infrared Fourier Transform Spectroscopy (DRIFTS) measurements were performed with a Bruker Vertex 70 spectrometer equipped with a flow-cell. The samples were placed in the sample holder. Prior to the measurements, the samples were heated under O_2 flow (10 mL/min) at 300 °C for 60 min. After the pre-treatment, the temperature of the samples was controlled, and C_2H_6 , N_2 , or O_2 were purged into the samples. The spectra were recorded.

2.4. Characterization

X-ray diffraction (XRD) patterns were recorded on a Bruker D8 Advance diffractor with $\text{Cu-K}\alpha$ ($\lambda = 1.5418 \text{ \AA}$) radiation at room temperature (tube voltage: 40 kV, tube current: 40 mA). Fourier Transform Infrared Spectrometer (FTIR) was conducted on a Bruker Vertex 70 spectrometer. X-ray photoelectron spectroscopy (XPS) was performed on a Thermo Scientific K-Alpha spectrometer. The binding energies were calibrated using the C_{1s} peak at 284.8 eV. Peak deconvolution for molybdenum oxidation (Mo^{6+}), vanadium oxidation state (V^{4+} and V^{5+}) and oxygen reduction state were conducted based on previous research [42]. Scanning electron microscopy (SEM) with energy-dispersive X-ray spectroscopy (EDX) analysis was carried out with an electron microscope (Sigma 300, Zeiss) equipped with an EDX detector (Oxford Xplore 50). Transmission electron microscope (TEM) with energy-dispersive X-ray spectroscopy (EDX) analysis was carried out with an JEOL JEM-F200 equipped with an EDX detector (JED-2300 T). Electron paramagnetic resonance (EPR) was carried out with a Bruker EMX PLUS. Differential scanning calorimetry (DSC) was carried out with NETZSCH DSC 200F3. The surface areas were measured by a Micromeritics 3flex sorption analyzer with N_2 adsorption-desorption measurements at –196 °C. The samples were evacuated at 200 °C for 2 h before the measurements.

Temperature programmed oxidation (TPO) measurements were carried out on Belcat II. Before the measurements, the material was pre-treated at 300 °C for 1 h in N_2 (25 mL/min) or in air (25 mL/min). The temperature was increased from 100 °C to 600 °C with a ramp of 10 °C/

min in O₂ flow (10 % of O₂ in He, 10 mL/min). The O₂ consumption during ramping step was measured by a thermal conductivity detector (TCD). C₂H₆ adsorption and temperature programmed desorption (TPD) measurements were carried out on Belcat II. Before the measurements, the material was pre-treated at 100 °C for 1 h in He (25 mL/min). The desorption profile from 100 °C to 600 °C was recorded with TCD under He flow (20 mL/min). Temperature programmed C₂H₆ reduction (TP-C₂H₆) tests were carried on ZVM and VM. Reaction conditions were as follow: catalyst weight; 0.5 g, reactant gas composition; C₂H₆/Ar=1/20 (mol%), total flow rate; 21 mL/min, reaction temperature range from 100 °C to 500 °C at a rate of 10 °C/min. The products were analyzed by FID and TCD. Elemental compositions in the bulk were measured by inductively coupled plasma atomic emission spectroscopy (ICP-AES) (Agilent 5110).

Rietveld refinement of ZVM was analyzed by the Rietveld diffraction program of GSAS. The initial structure was obtained from the previous reports [43]. All metal positions and pattern parameters were refined for obtaining the lowest *R*_{wp}. Atom positions are shown in Table S1.

2.5. Catalytic reaction

Catalytic tests for ODH of C₂H₆ were carried out in a conventional vertical flow system with a fixed bed flow reactor. The catalysts (0.5 g, granularity: 20–30) were charged in the fixed bed flow reactor. Before the reaction, pre-heating step was carried out at 310 °C under a various flow (air, N₂, and C₂H₆). Then, the reaction mixture of N₂/O₂/C₂H₆ with molar ratio of 40/5/5 (total flow rate: 50 mL/min) was fed to the reactor. The reactor was heated at a rate of 10 °C/min ranging from 260 °C to 310 °C, and these conditions were kept for 60 min at every 10 °C with analysis of the reactants and products. The reactants and products were analyzed with an online gas chromatograph (GC) GC-2014 C equipped with both FID and TCD detectors. C₂H₆ conversion, C₂H₄ yield, selectivity and CO_x selectivity were calculated based on the following equation:

$$\text{C}_2\text{H}_6 \text{ conversion (\%)} = \frac{\text{mole of C}_2\text{H}_6 \text{ reacted}}{\text{mole of C}_2\text{H}_6 \text{ fed}} \times 100\%$$

$$\text{C}_2\text{H}_4 \text{ yield (\%)} = \frac{\text{mole of C}_2\text{H}_4 \text{ produced}}{\text{mole of C}_2\text{H}_6 \text{ fed}} \times 100\%$$

$$\text{C}_2\text{H}_4 \text{ selectivity (\%)} = \frac{\text{mole of C}_2\text{H}_4 \text{ produced}}{\text{mole of C}_2\text{H}_6 \text{ reacted}} \times 100\%$$

$$\text{CO}_x \text{ selectivity (\%)} = \frac{\text{mole of CO}_x \text{ produced}}{\text{mole of C}_2\text{H}_6 \text{ reacted}} \times \frac{1}{2} \times 100\%$$

To investigate the reaction mechanism of C₂H₆ ODH, the stepwise reaction of C₂H₆ ODH was carried out over ZVM and VM. The detailed steps were as follows: First, 0.5 g of catalysts were charged in the fixed bed flow reactor and the pre-heating step was carried out at 310 °C under Ar for 1 h. Then, catalysts were treated under a gas flow of 5 % of C₂H₆/Ar, 5 % of O₂/Ar, and 5 % of C₂H₆/Ar at 310 °C in an alternating fashion, and the intensity of FID signal and TCD signal were recorded during the whole process. The carbon balance was over 97 % for each run.

2.6. Activation energy

Furthermore, in order to investigate the reason for difference of catalytic performance between ZVM and VM, the catalytic test was conducted at 250–265 °C, and the apparent activation energy was calculated by Arrhenius plots (Fig. S1). The catalytic rates can simplify to the following form of C₂H₆ ODH rates:

$$r_{ODH} = k \times P_{O_2}^a \times P_{C_2H_6}^b$$

where a and b represent the reaction order of O₂ and C₂H₆ and k

represent the reaction rate constant, respectively. C₂H₆ ODH rates as a function of O₂ pressure to the power of a and C₂H₆ pressure to the power of b on catalysts are shown in Fig. S2. Regressing the obtained a and b to the form of C₂H₆ ODH rates and thus get the reaction rate constant (k).

The apparent activation energy can be expressed in the form Arrhenius equation:

$$\ln k = \frac{-E_a}{RT} + \ln A$$

The lnk values derived from measured reaction rate constant (k) for C₂H₆ on catalysts as a function of reciprocal temperatures are shown in Fig. S1. Regressing of obtained data to the form of Arrhenius equation and get apparent activation energy. The transport limitations and estimation errors are found to be negligible in the previous literature by using the method of Koros and Nowak [44,45] using the catalyst with the same crystalline structure of ZVM.

2.7. Modeling and simulation

Static binding energy and transition state energy were conducted on Density functional theory (DFT) calculations. Optimizing the structures of the materials was carried out with Vienna Ab initio Simulation Package (VASP) [46,47]. The PBE exchange-correlation functional based on generalized gradient approximation was employed [48]. The Plane wave basis sets used to approximate wave functions of valence electrons were included to a 400 eV kinetic energy cut-off. The projector-augmented wave (PAW) method was adopted to describe interactions between valence electrons and atom cores [49]. All calculations were spin-polarized. Gaussian smearing with a width of 0.1 eV was imposed for electron distributions near the Fermi Level. The electronic structures and geometries of structures were optimized until the energy differences between successive steps were less than 1 × 10⁻⁴ eV and 1 × 10⁻³ eV respectively. For modeling the dispersion interactions, the DFT-D3 method was adopted [50]. The number of layers is two because the van der Waals interaction between C₂H₆ in two neighboring layers was negligible (Fig. S3). The 1 × 1 × 2 unit cell used for simulation. The 1 × 1 unit cell with a corresponding 1 × 1 × 2 Gamma k-point mesh generated by post-processing VASPkit package was used [51,52]. The reaction of C₂H₆ ODH was simulated in the heptagonal channel, which was in good agreement with the previous literature [53,54]. The charge densities difference was calculated using the VASPkit package. Complete linear synchronous transit (LST) method was adopted to generate an initial pathway from the reactant to the product in the unit cell [55]. The barrier energies were obtained using the climbing image nudged elastic band (clNEB) method [56,57]. Activation energy calculation predicted the energy difference between the transition state and the energy of the system with molecule in the cavity.

$$\Delta E_t = E_{ts} - E_{(\text{material} + \text{molecule})}$$

where ΔE_t is the activation energy based on DFT calculation, E_{ts} is the energy of transition state, and $E_{(\text{material} + \text{molecule})}$ is the energy of the material with adsorbed molecule.

3. Results and discussion

3.1. Materials synthesis and characterization

ZVM was synthesized using a hydrothermal method. A soluble Mo source of MAHM was prepared by dissolving MoO₃ in an aqueous solution of methylamine. VOSO₄ was used as the V source and added to the MAHM solution. ZnSO₄·7 H₂O was also added to the mixture. After the hydrothermal synthesis, the resulting raw solid was purified using a 0.4 mol/L aqueous solution of oxalic acid at 60 °C. This process yielded well-crystallized ZVM.

The XRD patterns of ZVM and VM are shown in Fig. 1 A. The XRD pattern of ZVM exhibited characteristic peaks at (020), (120), (210),

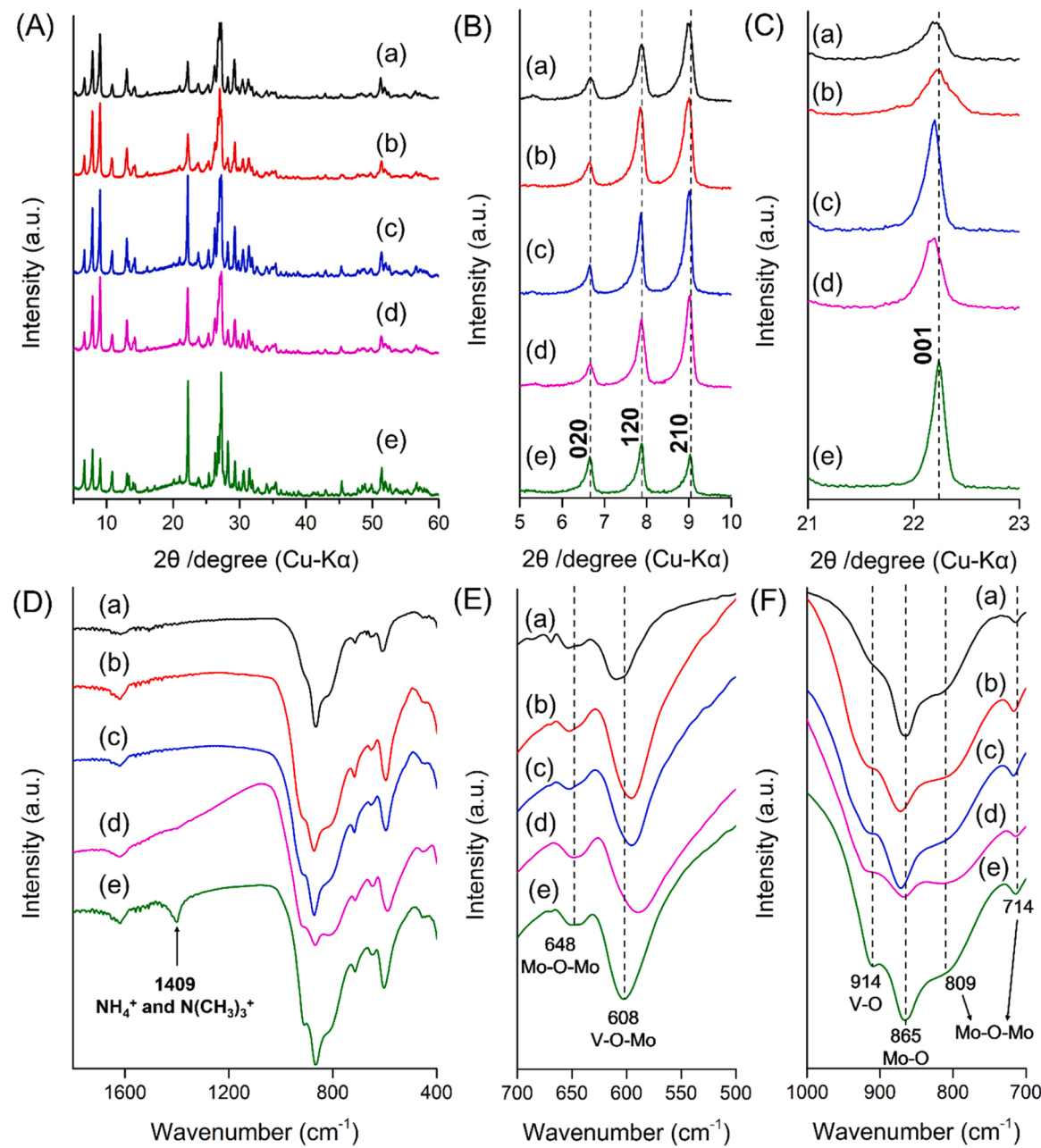


Fig. 1. (A) XRD patterns, (B) enlarged patterns in 5–10 degree, (C) enlarged patterns in 21–23 degree, (D) FTIR spectra, (E) enlarged FTIR spectra in 700–500 cm^{-1} , and (F) enlarged FTIR spectra in 1000–700 cm^{-1} of (a) ZVM, (b) ZVM-N300, (c) ZVM-A300, (d) ZVM-E300, and (e) VM.

(001), and other positions that were consistent with those of the crystalline orthorhombic VM (Fig. 1B) [41]. These results confirmed that the crystalline structure of ZVM and VM was the same. There was a new diffraction peak at 5.3 degree attributed to the (110) plane, which might be caused by Zn incorporation. The observed peak shift to a lower angle of ZVM suggested that the lattice parameter of ZVM was slightly larger than that of VM (Fig. 1B,C), which indicated that incorporating Zn into the VM framework caused expansion of the lattice parameter (Table S2).

The FTIR spectra of ZVM and VM showed that the peaks at 914 cm^{-1} attributing to V-O, 865 cm^{-1} attributing to Mo-O, 809, 714, and 648 cm^{-1} attributing to Mo-O-Mo, and 608 cm^{-1} attributing to V-O-Mo, respectively (Fig. 1 C) [40]. The IR bands below 1000 cm^{-1} of ZVM and VM were similar, suggesting a similar bonding state between the materials. However, a shift in the IR band at ca. 608 cm^{-1} was observed in ZVM, indicating a change in the bonding state due to Zn incorporation

(Fig. 1D). The IR band at about 1400–1409 cm^{-1} , attributed to NH_4^+ and $\text{N}(\text{CH}_3)_3^+$, originating from the metal precursor salts, was not observed in ZVM, which indicated that there was almost no NH_4^+ and $\text{N}(\text{CH}_3)_3^+$ in ZVM. Zn probably replaced NH_4^+ and $\text{N}(\text{CH}_3)_3^+$.

ZVM and VM were characterized by SEM, showing that both materials exhibited a rod shape with the size of ca. 100 nm in a diameter and varying lengths (Fig. 2A,B). Zn incorporation in VM did not change the morphology of the material. Elemental distribution of the material was characterized by SEM-EDX mapping. The result showed that Mo, V, and Zn were uniformly distributed within the crystal particle (Fig. 2C,D,F), indicating that Zn was incorporated intrinsically into the structure. Elemental composition of the material was calculated based on ICP-AES. The result showed that Mo: V: Zn = 1: 0.322: 0.036.

XPS analysis was conducted to confirm the oxidation state of the metal elements in ZVM (Fig. 3). The XPS spectra of Mo showed peaks at

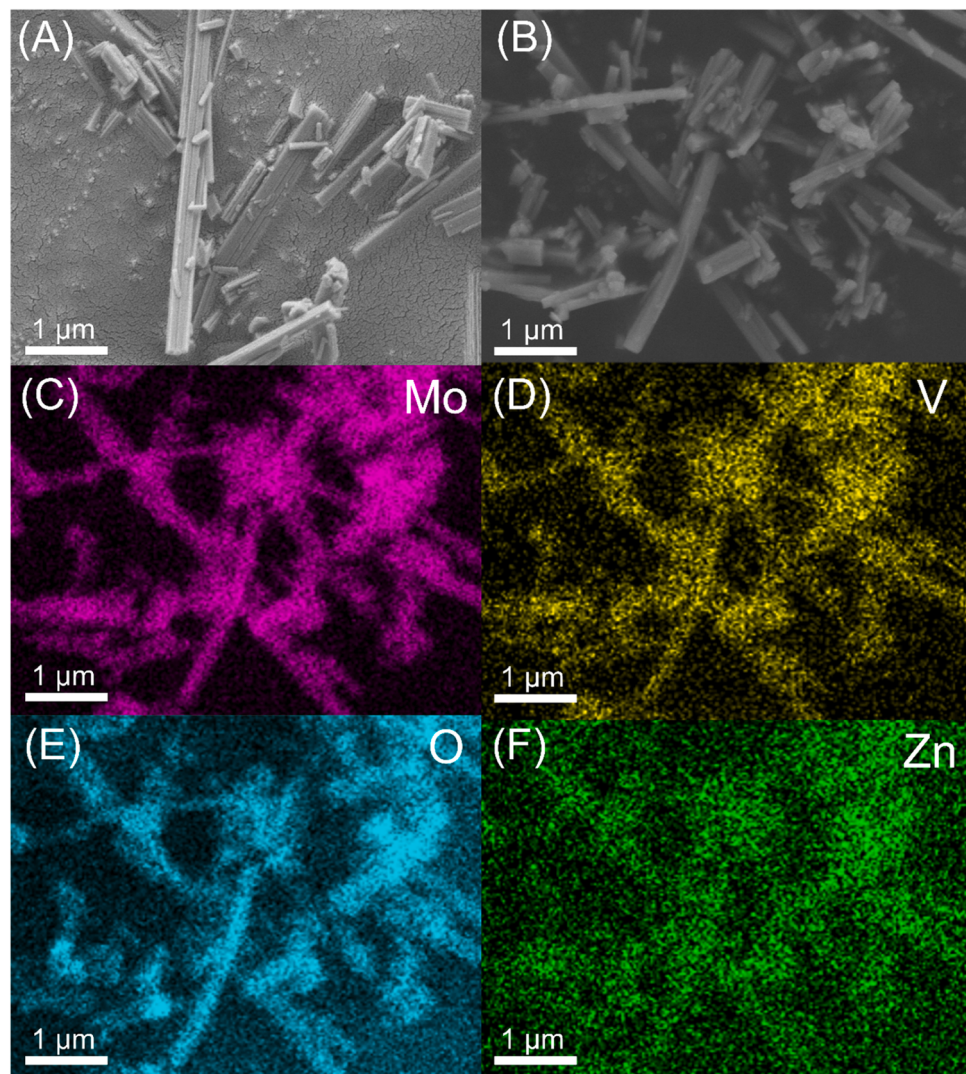


Fig. 2. SEM image of (A) VM, SEM image of (B) ZVM and corresponding elemental mapping images of (C) Mo, (D) V, (E) O, and (F) Zn.

ca. 232.9 eV and ca. 236.0 eV, corresponding to Mo ($3d_{5/2}$) and Mo ($3d_{3/2}$), respectively (Fig. 3Aa). These peaks indicated that the Mo species was primarily in the +6 oxidation state [58]. The corresponding V profile was fitted by two simulated peaks at ca. 516.4 eV and ca. 517.4 eV (Fig. 3B), attributing to V^{4+} and V^{5+} [59]. The ratio of V^{5+}/V^{4+} in ZVM was 0.50, which was higher than that in VM (0.38) (Fig. 3Ba,f). Zn was Zn^{2+} in ZVM. Based on the elemental analysis and oxidation states analysis, the chemical formula of the material was proposed to be $Zn_{1.1}^{2+}[Mo_{30}^{6+}V_{6.6}^{4+}V_{3.4}^{5+}O_{112.8}] \cdot 9 H_2O$.

The position of Zn in ZVM was determined by the Rietveld refinement combined with DFT calculation. The good agreement between the simulated XRD pattern and the experimental pattern obtained from Rietveld refinement demonstrated that the proposed structures were correct (Fig. 4). Atomic position of ZVM after Rietveld refinement was shown in Table S1. There were majorly two positions in the material for locating Zn, the heptagonal channel (site 1, 2, 3, 4, 5, 6, and 7) and the hexagonal channel (site 8, 9, 10, 11, 12, and 13) (Fig. 4A). The refinement indicated that Zn was in the heptagonal channel of the material. The energies of the material with Zn in different positions in the heptagonal channel and hexagonal channel were evaluated by the DFT calculation (Fig. 4C). When Zn located in site 1, the system energy was the lowest, indicating that the site was the most possible site for Zn location (Fig. 4C). Zn located in the heptagonal channel and embedded in the wall of the micropore.

The thermal stability of ZVM was evaluated by heating it under various conditions. ZVM was found to be stable in both air and N_2 at 400 °C, as evidenced by the unchanged XRD patterns and FTIR spectra after treatment (Fig. S4). While heating ZVM in H_2 at 400 °C resulted in damage to its crystalline phase, reducing the treatment temperature to 300 °C preserved the crystalline phase.

The microporosity of ZVM was studied by the N_2 adsorption-desorption and CO_2 adsorption-desorption measurements (Fig. S5). The BET surface area, external surface area, and the micropore volume (Table S2) were calculated based on the adsorption isotherms of CO_2 . The adsorbed volume of CO_2 of ZVM was similar to that of VM, confirming that the presence of Zn would not block the micropore of the material. Increasing the Zn content in the synthesis did not change the adsorption volume of CO_2 , and the micropore was not blocked (Fig. S5).

Furthermore, the Zn content was able to be varied by controlling the Zn content of the precursor solution. The results showed that the orthorhombic phase formed for Zn content (molar ratio of Zn to V in the precursor solution) of 0.15, 0.20, 0.25, and 0.30 (Fig. S6). Further increasing the Zn content or decreasing the Zn content would cause the generation of amorphous phase, such as the catalysts with the Zn content of 0.10 and 0.40 (Fig. S6Aa,f). Additionally, the V content was modulated by adjusting the V concentration in the precursor solution. The orthorhombic phase was synthesized with V content (molar ratio of V to Mo in the precursor solution) of 0.35, 0.40, 0.45, 0.50, 0.55, and

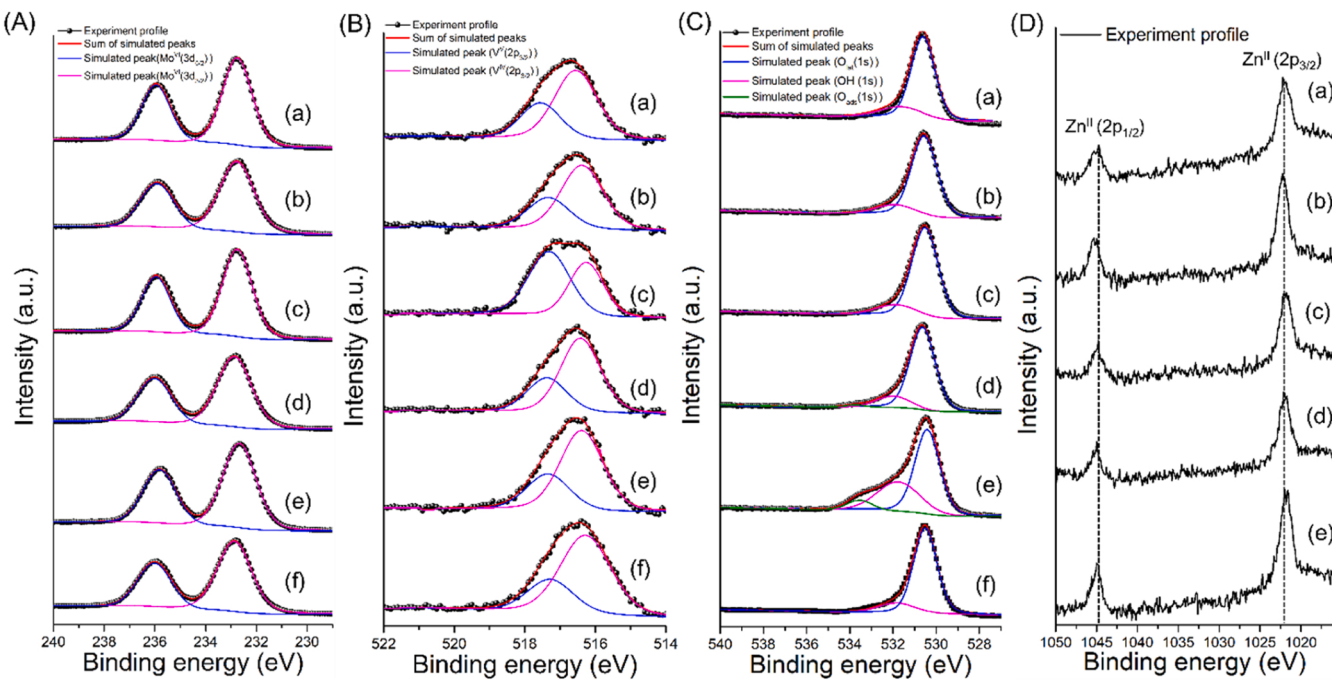


Fig. 3. XPS of (A) Mo of (a) ZVM, (b) ZVM-N300, (c) ZVM-A300, (d) ZVM-E300, (e) ZVM-AE300, and (f) VM, (B) V of (a) ZVM, $V^{5+}/V^{4+}=0.50$, (b) ZVM-N300, $V^{5+}/V^{4+}=0.48$, (c) ZVM-A300, $V^{5+}/V^{4+}=1.44$, (d) ZVM-E300, $V^{5+}/V^{4+}=0.46$, (e) ZVM-AE300, $V^{5+}/V^{4+}=0.45$, and (f) VM, $V^{5+}/V^{4+}=0.38$, (C) O of (a) ZVM, $O_{\text{lat}}/\text{OH} = 1/0.140$, (b) ZVM-N300, $O_{\text{lat}}/\text{OH} = 1/0.150$, (c) ZVM-A300, $O_{\text{lat}}/\text{OH} = 1/0.146$, (d) ZVM-E300, $O_{\text{lat}}/\text{OH}/O_{\text{ads}} = 1/0.167/0.015$, (e) ZVM-AE300, $O_{\text{lat}}/\text{OH}/O_{\text{ads}} = 1/0.556/0.104$, and (f) VM, $O_{\text{lat}}/\text{OH} = 1/0.145$, (D) Zn of (a) ZVM, (b) ZVM-N300, (c) ZVM-A300, (d) ZVM-E300, (e) ZVM-AE300.

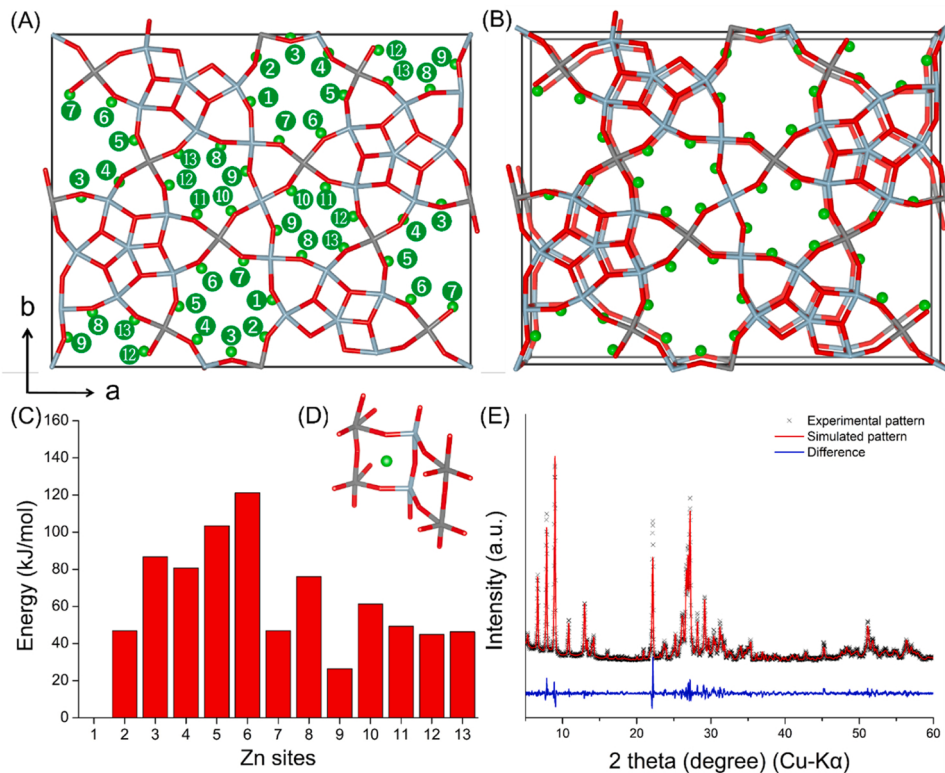


Fig. 4. Structure models of (A) and (B) VM framework with different sites for locating Zn, (C) relative energy of Zn in different sites, (D) enlarged model of Zn location, and (E) Comparison of the simulated XRD based on the Rietveld refinement with the experimental XRD with $R_{\text{wp}} = 11.05\%$, Mo (blue), V (gray), O (red), Zn (green).

0.60 (Fig. S7). Excessive or low V content prevented the formation of crystals, such as the catalysts with V content of 0.35 and 0.60 (Fig. S7Aa, f).

3.2. C_2H_6 oxidation to C_2H_4

C_2H_6 ODH was carried out over the ZVM catalyst at each reaction temperature under atmospheric pressure. The activity of the reaction increased with the reaction temperature (Fig. 5A,B). The conversion of C_2H_6 over the catalyst was low (16 %) at a low reaction temperature ($260^\circ C$), and the selectivity to C_2H_4 was over 95 %. The conversion increased with the increase in reaction temperature. C_2H_6 conversion of 49 % was achieved with C_2H_4 selectivity of 92 % at $300^\circ C$, finally. Compared with VM, ZVM exhibited higher activity over the entire selected temperature range, although both of them possessing the orthorhombic structure. The result demonstrated that Zn significantly enhanced the catalytic activity of the catalyst.

Zn was found to be critical for achieving high activity in the reaction. The C_2H_6 ODH was catalyzed by ZVM with varying Zn contents at $310^\circ C$ (Fig. S8). Increasing the Zn content of the catalyst within a certain range increased the C_2H_6 conversion, while excessive or low Zn content decreased reaction activity with keeping almost the same selectivity to C_2H_4 (Fig. S8). The results highlight the importance of Zn in the reaction.

A VM supported Zn catalyst, Zn-VM, was synthesized using an impregnation method (see experimental for details) with almost the same Zn content to ZVM. XRD and FTIR of Zn-VM were unchanged compared to those of VM (Fig. S9A,B), indicating that impregnating Zn did not alter the structure of VM. There was no obvious particle being

observed in TEM image, and Zn signal was uniform in EDX-mapping, demonstrating that Zn was well-dispersed on VM (Fig. S10). The C_2H_6 ODH activity of Zn-VM was lower than that of both ZVM and VM, suggesting that Zn on the external surface of VM did not activate VM (Fig. S9C,D). Further increasing the loading amount of Zn did not lead to increase the activity (Fig. S9).

V also affected the catalytic activity. ZVM with different V contents was synthesized. The reaction was carried out at $310^\circ C$. The selectivity to C_2H_4 decreased with increasing the V content of the catalysts while kept almost the same C_2H_6 conversion (Fig. S11).

The pre-treatment condition affected the catalytic activity of ZVM. ZVM was treated in N_2 , air, and C_2H_6 for 2 h at $300^\circ C$, forming ZVM-N300, ZVM-A300, and ZVM-E300 (Fig. 1). Although the crystal structure of the catalyst was maintained after the treatments, the catalytic activity slightly changed. The catalytic activity of ZVM-A300 decreased slightly, while the activity of ZVM treated with N_2 and C_2H_6 increased (Fig. 5A,B).

The stability of the catalyst was further tested for ZVM. The reaction was carried out for 35 h at $300^\circ C$ (Fig. 5C). The result showed that within the first 10 h the conversion of C_2H_6 slightly decreased from 56 % to 50 %, while the selectivity to C_2H_4 gradually increased from 84 % to 90 %. The yield of C_2H_4 almost did not change in the first 10 h. After 10 h, the conversion of C_2H_6 and selectivity to C_2H_4 almost remained to be ca. 49% and 92%, indicating that the catalyst was stable. After the reaction, the catalyst was characterized by XRD, SEM, and XPS. XRD showed that the characteristic peaks of orthorhombic phase did not change after the catalytic reaction, indicating that the crystalline phase of the catalyst did not change (Fig. 5D). SEM showed that the morphology of the catalyst also did not change, remaining the rod-shape

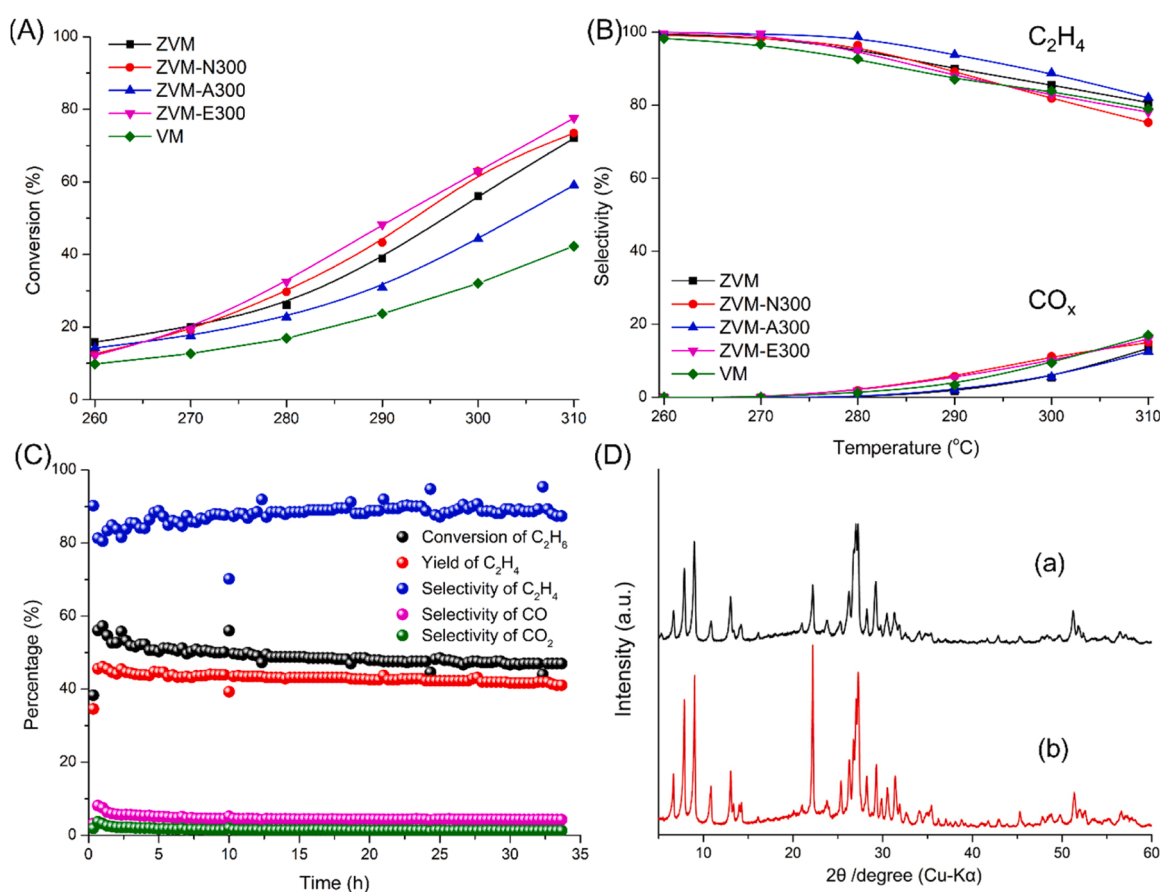


Fig. 5. C_2H_6 conversion (A) and product selectivity (B) of ZVM, ZVM-N300, ZVM-A300, ZVM-E300, and VM at different temperatures, (C) long-term stability of ZVM, (D) XRD patterns of (a) ZVM and (b) ZVM after the catalytic reaction, reaction conditions: 0.5 g of catalyst, 50 mL/min of total flow, $C_2H_6/O_2/N_2 = 5/5/40$, 260–310 °C of reaction temperature for (A) and (B), 300 °C of reaction temperature for (C), the carbon balance of all catalytic reactions being over 97 %.

(Fig. S12). XPS of the catalyst after the reaction (Fig. S13) revealed that the valences of Mo, V, and Zn almost did not change while OH content slightly increased. Additionally, the recyclability of the catalyst was also tested, which demonstrated that the catalyst could be reused (Fig. S14).

Compared with the reported C₂H₆ ODH catalysts, ZVM displayed superior performance. ZVM exhibited the highest yield of C₂H₆ at the lowest temperature among the reported catalysts (Fig. S15 and Table S3).

3.3. Reaction mechanism

The ODH of C₂H₆ was conducted in a stepwise reaction to understand the reaction mechanism (Fig. 6A). Initially, ZVM was pretreated with Ar at 310 °C, followed by sequential purging of C₂H₆, O₂, and C₂H₆ at the same temperature. Ar purging was employed to remove any residual gases from the catalyst. The as-synthesized ZVM did not react with C₂H₆ at 310 °C, as the C₂H₆ signal was quickly detected upon introduction. When O₂ was purged through the catalyst, the O₂ signal was not observed for the first 20 min, indicating that O₂ was consumed to oxidize ZVM. After O₂ purging, C₂H₆ was reintroduced, resulting in detection of both C₂H₄ and CO signals, which gradually decreased as the reaction time was extended. In this stage, the oxidized ZVM reacted with C₂H₆, primarily forming C₂H₄ and CO. The same experiment was conducted for VM (Fig. 6B). The phenomenon observed when VM was used as the catalyst was similar to that of ZVM, suggesting that the reaction mechanism might be the same. The difference was the reaction rate. O₂ (8 min) and C₂H₆ (3 min) were detected more rapidly than the case of ZVM, when they were introduced. Less C₂H₄ but more CO were observed

compared to the case of ZVM. This indicated that Zn might not only activate C₂H₆ but also O₂.

XPS analysis was conducted on ZVM with different treatments to know the changes in the oxidation state of Mo, V, and Zn in ZVM (Fig. 3). ZVM was treated in N₂, air, and C₂H₆ at 300 °C. Mo was majorly Mo⁶⁺ in ZVM-N300 (Fig. 3Ab), and V was in the mixture of V⁵⁺ and V⁴⁺ with a ratio of 0.48 in ZVM-N300 (Fig. 3Bb). After calcination in air at 300 °C to form ZVM-A300, the peak of V⁵⁺ increased obviously with the ratio of V⁵⁺/V⁴⁺ = 1.44 (Fig. 3Bc). The oxidation state of Mo and Zn did not change after calcination at 300 °C. Following the air treatment, C₂H₆ was used to treat ZVM-A300, and the results indicated that V⁵⁺ was reduced to V⁴⁺ without any changes in Mo and Zn. Therefore, only V underwent a change in oxidation state during the reaction. Thus, the redox of V from V⁴⁺ to V⁵⁺ was crucial in achieving high activity for C₂H₆ ODH. To further confirm the importance of V⁵⁺ for C₂H₆ ODH, ZVM-A300 (0.5 g) was treated with an aqueous solution of N₂H₆SO₄ (0.25 mol/L, 15 mL) at room temperature to reduce V⁵⁺, and the resulting catalyst was denoted as ZVM-A300-N₂H₆. XRD and FTIR showed that the basic structure of ZVM-A300 did not change (Fig. S16). XPS showed that V valence changed from V⁵⁺ to V⁴⁺ without change of O (Fig. S17). This indicated that oxygen species of ZVM-A300 and ZVM-A300-N₂H₆ were the same. The only difference was V valence. ZVM-A300-N₂H₆ did not react with C₂H₆ (Fig. S18), demonstrating that V⁵⁺ was critical for C₂H₆ ODH. The previous studies showed that V species are the active sites for the first C-H bond activation in C₂H₆ activation [60–62], while Mo does not significantly impact on C₂H₆ activation [63], which is in good agreement with our results.

Furthermore, the XPS peak of O_{1s} could be fitted with the peaks at

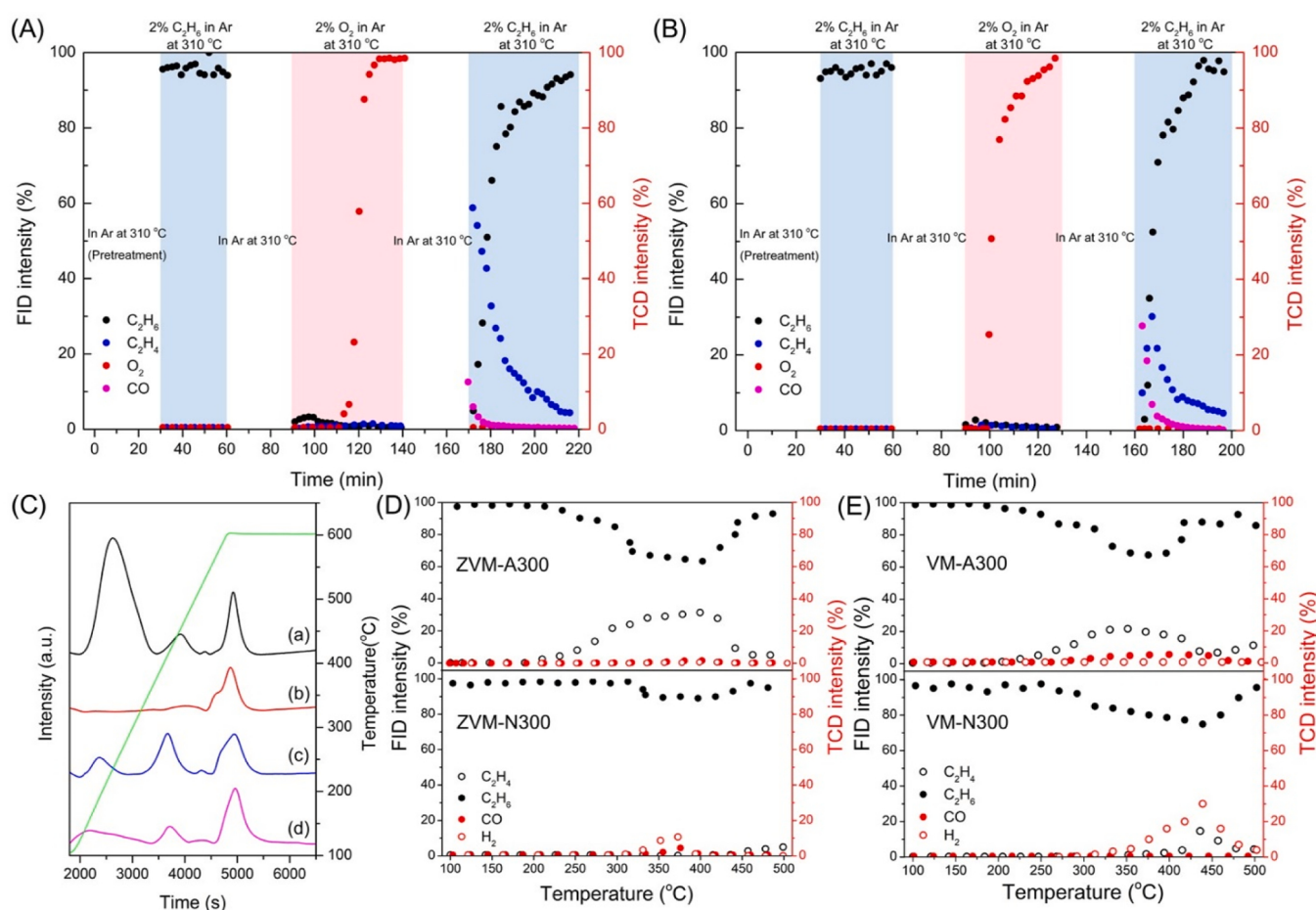


Fig. 6. The stepwise reaction of C₂H₆ ODH catalyzed by (A) ZVM and (B) VM, reaction condition: catalyst 0.5 g, Ar 30 mL/min, (C) TPO profiles of (a) ZVM-N300, (b) ZVM-A300, (c) VM-N300, and (d) VM-A300, (D) TP-C₂H₆ profiles of ZVM-A300 and ZVM-N300, and (E) TP-C₂H₆ profiles of VM-A300 and VM-N300.

530.35 eV, 531.6 eV, and 533.5 eV, corresponding to lattice oxygen (O_{lat}), lattice OH (OH), and adsorption oxygen (O_{ads}) in the material (Fig. 3C) [58]. There was majorly lattice O_{lat} with only few OH being observed in ZVM-N300 (Fig. 3Cb). After the oxidation of ZVM at 300 °C in air, the peak areas and positions of O_{lat} and OH remained unchanged, indicating saturation of lattice oxygen in the fresh catalyst (Fig. 3Cc). When the catalyst was treated with C_2H_6 , the peak of OH appeared, indicating the formation of OH (Fig. 3 Cd) [64]. ZVM-A300 was treated with C_2H_6 and the resulting catalyst (ZVM-AE300) showed the obvious OH and O_{ads} signals (Fig. 3Ce), demonstrating that C_2H_6 dehydrogenation occurred on ZVM-A300. OH formed by transferring H from C_2H_6 to O_{lat} with forming some oxidized organic species as O_{ads} . The FTIR peak at 3560 cm^{-1} of ZVM and VM was attributed to O-H, which was in good agreement with XPS (Fig. S19). TPD of ZVM-E300 revealed that there were three main peaks with the positions at 220, 460, and 520 °C (Fig. S20). The presence of the desorption indicated the dehydration of OH at the temperatures forming the oxygen vacancies (O_v). At the current reaction temperature (260–310 °C), only partial OH was able to be transferred to O_v . The results demonstrated that when C_2H_6 reacted with the catalyst, O_{lat} of the catalyst transferred to OH, which then dehydrated to form O_v . The existence of O_v after the catalyst was treated with C_2H_6 was further confirmed by EPR, showing the peak at 3510 G with g of 2.0046 attributed to O_v (Fig. S21A).

Furthermore, in situ FTIR measurements were carried out for ZVM-A300 and VM-A300 at 300 °C (Fig. 7A,B). After introducing C_2H_6 , the bands at 2800–3100 cm^{-1} and 1250–1650 cm^{-1} corresponded to C-H stretching mode and bending mode of C_2H_6 , respectively. The bands at 3251, 3325, and 3560 cm^{-1} were attributed to OH attached to the metal ions (M-OH), which were derived from dehydrogenating C_2H_6 with the catalysts (Fig. 7A) [65–67]. Notably, in comparison to VM, the peak at

3325 cm^{-1} was exclusive in ZVM, possibly indicating OH binding to Zn. Upon saturation with C_2H_6 , N_2 was introduced for C_2H_6 desorption, revealing that the bands for C_2H_6 obviously decreased, indicating that the free C_2H_6 was removed by N_2 purging. However, the remaining peaks for OH indicated that OH could not be removed completely by N_2 . The persistence of C-H bond peaks suggested the formation of intermediates strongly bound to the catalysts. The position of peak at 1540 cm^{-1} for the C-H bond in ZVM was different from that in VM, indicating that intermediates interacted with Zn in a distinct binding state compared to the case of VM. After O_2 purging, all the remaining peaks disappeared, indicating that OH was disappeared which might be transferred to O_{lat} and the intermediates were removed from the catalysts by O_2 . The in situ FTIR demonstrated the formation of intermediates during the reaction and O_{lat} would be recovered by O_2 .

To test whether any reactive oxygen species, such as $\cdot O_2$ and $\cdot OH$, were generated during air calcination, the quenching experiment was conducted. $CHCl_3$ and isopropanol (IPA) were used to quench $\cdot O_2$ and $\cdot OH$ [68,69], respectively. ZVM-A300 (0.5 g) was treated with $CHCl_3$ (10 mL) followed by treatment with a 10 % IPA aqueous solution (1.66 mol/L, 200 mL). The resulting catalyst was denoted as ZVM-A300-quencher. XRD and FTIR of ZVM-A300-quencher were almost the same to those of ZVM-A300, indicating that the structure of the catalyst remained unchanged after the quenching experiment (Fig. S22). C_2H_6 oxidation by ZVM-A300-quencher showed that C_2H_6 was consumed at the beginning and the performance of ZVM-A300-quencher was similar to that of ZVM-A300, demonstrating that the quenching experiment did not affect the activity of the catalyst (Fig. S23). Moreover, ZVM-A300 was characterized by EPR (Fig. S21B), showing that reactive oxygen species was essentially absent from the catalyst. Therefore, there was no reactive active species generated [70,

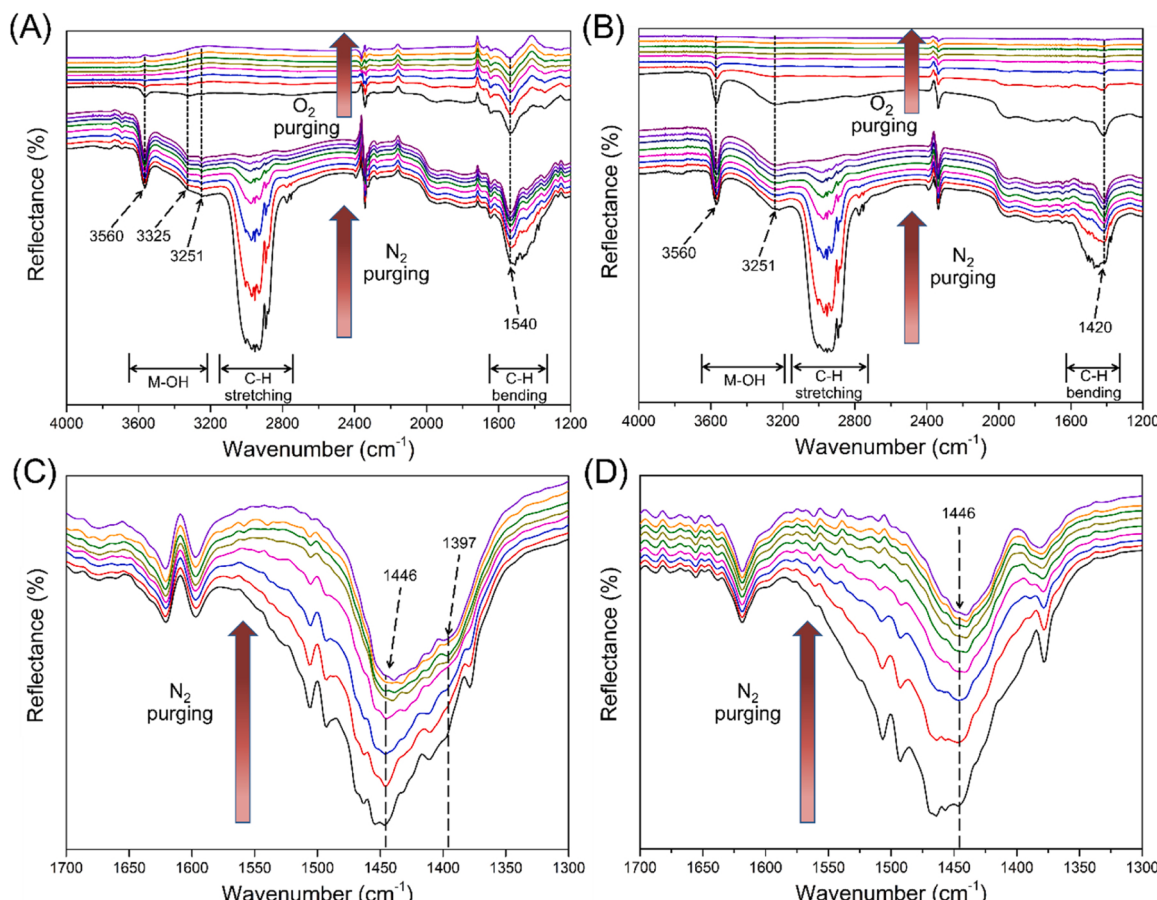


Fig. 7. In situ FTIR of C_2H_6 in (A) ZVM and (B) VM at 300 °C under N_2 flow or O_2 flow, in situ FTIR of C_2H_6 on (C) ZVM and (D) VM at 25 °C under N_2 flow.

71].

Based on the results presented above, a reaction pathway was proposed. The reaction mechanism of ZVM for C_2H_6 ODH was similar to Mars-Van Krevelen (MvK) Mechanism [33,72–75]. The as-synthesized ZVM was oxidized by O_2 to form the oxidized ZVM with increasing the valence of V^{4+} to V^{5+} . The oxidized ZVM extracted H from C_2H_6 to form intermediates that bound to the catalyst, forming OH that were bound to the framework of ZVM. The intermediates then decomposed to produce C_2H_4 , and V in ZVM was subsequently reduced to V^{4+} again (Fig. 8A). OH might dehydrate with H to form O_v on the catalyst, which was able to be recovered by O_2 oxidation. The proposed reaction mechanism of ZVM was similar to that of the most of reported Mo and V based C_2H_6 ODH catalysts (Table S4).

To confirm the role of Zn, TPO and TP-C₂H₆ were conducted for ZVM. The redox property of the material was investigated by TPO (Fig. 6C). In the TPO profiles of ZVM-N300 and VM-N300, three main

peaks were observed at 270, 400, and 600 °C, corresponding to three different reductive species in the catalysts. The reduction species at 270 °C were related to C_2H_6 ODH, given its proximity to the reaction temperature. Compared with VM, the peak of ZVM-N300 at 270 °C was larger, which indicated that the incorporation of Zn activated O_2 and facilitated the oxidation of more reductive species at a low temperature (270 °C). Furthermore, TPO investigations were conducted using ZVM-A300 and VM-A300. The result showed that the peak at 270 °C disappeared, indicating that the species was oxidized under calcination at 300 °C while the peak at 400 and 600 °C remained unchanged. From XPS, V^{4+} was oxidized to V^{5+} at 300 °C (Fig. 3B), and thus the TPO peak at 270 °C was attributed to the oxidation of V^{4+} . TPO of ZVM-E300 and VM-E300, the peak at 200–300 °C of ZVM-E300 was at a lower temperature, indicating that Zn incorporation might activate O_2 , which caused easier oxidation of the reduced catalysts (Fig. S24). DSC confirmed that the reactions between O_2 and the catalysts were

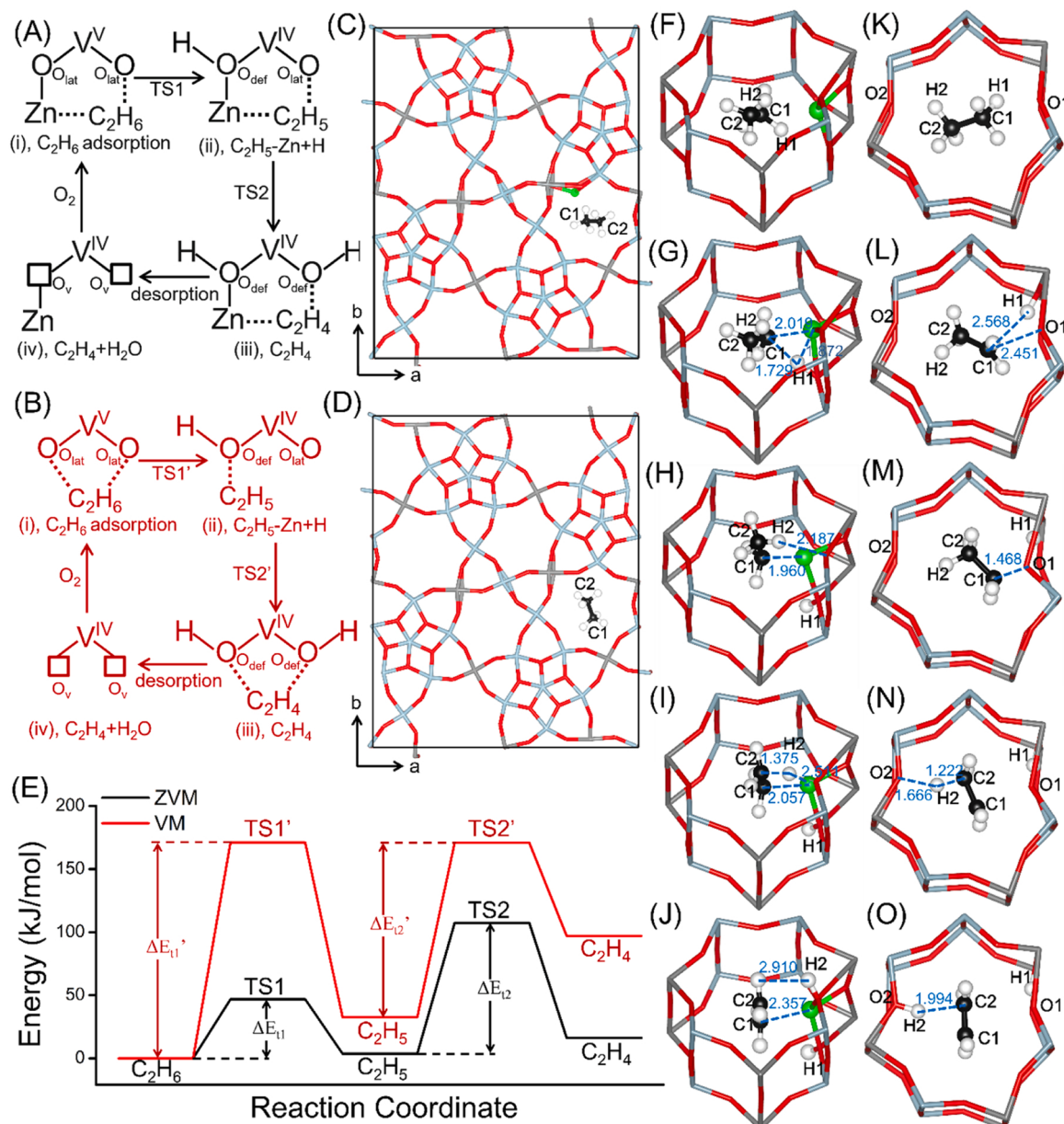


Fig. 8. Proposed reaction pathway of C_2H_6 ODH catalyzed by (A) ZVM and (B) VM, (C) C_2H_6 in unit cell of ZVM, (D) C_2H_6 in unit cell of VM, (E) energies of the intermediates and the transition states of C_2H_6 dehydrogenation based on DFT calculations, structure models of the intermediates and the transition states of C_2H_6 dehydrogenation, (F) C_2H_6 in ZVM, (G) TS1 in ZVM, (H) C_2H_5 in ZVM, (I) TS2 in ZVM, (J) C_2H_4 in ZVM, (K) C_2H_6 in VM, (L) TS1' in VM; (M) C_2H_5 in VM, (N) TS2' in VM, (O) C_2H_4 in VM. Mo (blue), V (gray), O (red), Zn (green), C (black), H (white).

exothermic, with ZVM exhibiting a higher heat release compared to VM, indicating that ZVM preferentially reacted with O₂ (Fig. S25). Therefore, Zn caused oxidizing V⁴⁺ in the material at a low temperature much easier (270 °C).

The interaction of O₂ and the catalysts was simulated by the DFT calculation. The charge density difference (CDD) of O₂ adsorbed in the heptagonal channel of the catalysts were calculated (Fig. 9). An increase in charge density was observed between Zn and O while a decrease in charge density was observed between O-O or O₂, indicating that the O-O bond was weakened in ZVM (Fig. 9A,B). In the case of VM, although O₂ also located in the heptagonal channel, the charge density was much smaller than in the case of ZVM, indicating that O₂ was weakly affected by VM (Fig. 9C,D). Therefore, Zn caused activation of O₂, leading to oxidation of V⁴⁺ in the material at a low temperature.

TP-C₂H₆ were conducted (Fig. 6D, E). For ZVM-N300, there were no C₂H₆ signal decreases in the TP-C₂H₆ profiles at 200 °C, demonstrating that C₂H₆ did not react with the catalyst at low temperatures. Further increasing the temperature to over 320 °C caused the catalyst to react with C₂H₆, possibly due to the reaction between O_{lat} of the catalyst and C₂H₆. ZVM-N300 was not active for reacting with C₂H₆ at low temperatures. Air treatment activated the catalyst. ZVM-A300 showed a decrease in the C₂H₆ signal at 200 °C, along with the appearance of products peaks of C₂H₄ and CO, indicating that the catalyst reacted with C₂H₆ at low temperatures. Similar to ZVM-N300, VM-N300 did not show the peak at low temperatures, and only VM-A300 showed the signal. The peak of VM-A300 was smaller than that of ZVM-A300, indicating that Zn also activated C₂H₆.

The charge density difference (CDD) of C₂H₆ in the micropores of the catalysts was calculated, showing the charge enrichment and depletion of C₂H₆ after adsorption (Fig. 9). The charge density between C of C₂H₆ and Zn of the catalyst increased, while it decreased between the C-H bond of C₂H₆ (Fig. 9E, F). This indicated that the C-H bond of C₂H₆ was weakened due to interaction with Zn. For VM, the charge densities of both charge increasing and decreasing were smaller, indicating weak interaction between C₂H₆ and VM (Fig. 9G, H). Moreover, the in situ FTIR spectra of C₂H₆ in ZVM and VM at 25 °C showed that the peak shifted to a lower wavenumber (1397 cm⁻¹) in ZVM (Fig. 7C,D), indicating that the C-H bond of C₂H₆ in ZVM was longer than that in VM. This also indicated that the C-H bond was weakened by ZVM. CDD also showed that the charge density of O nearby Zn increased, indicating that H affinity of O increased after Zn incorporation, which enhanced the activity of dehydrogenation (Fig. S26).

To further understand the role of Zn during the reaction, we investigated the structures of the intermediates and transition states at each

step of C₂H₆ ODH over ZVM and VM (Fig. 8). The structure of ZVM and VM were optimized. The catalytic reaction occurred within the heptagonal channel of the catalysts [53]. The energies and structures of intermediates and transition states of C₂H₆ inside the heptagonal channel were obtained. The static binding energy was calculated using PBE and PBE-D3 correction. With D3 correction, the system energy decreased further, indicating the presence of van der Waals interactions between the catalyst and C₂H₆ (Fig. S27).

According to the above discussion, H of C₂H₆ was extracted by the catalyst and migrated to the framework of the catalyst. The exact position of H was estimated by the DFT calculation. The result showed that H at V-OH revealed obviously lower energy (Fig. S28), indicating that these sites were suitable for H extraction.

For ZVM, adsorbed C₂H₆ was located nearby Zn in the heptagonal channel of the catalyst (Fig. 8C). According to the CDD images, the C-H bond was weakened in the catalyst by interacting with Zn (Fig. 9E, F). Dehydrogenation of C₂H₆ occurred with substring H1 from C₂H₆ to the O atom of the framework, forming the intermediate of C₂H₅ coordinating to Zn with a distance of C1-Zn of 1.960 Å (Fig. 8H). The energy of the intermediate increased to 3.7 kJ/mol (Fig. 8E). The transition state (TS1) was optimized. H1 interacted with C₂H₅ and Zn with distances of C1-H1 and H1-Zn of 1.729 and 1.872 Å, and C1 interacted with Zn at a distance of 2.019 Å (Fig. 8G). Zn assisted in transferring H from C₂H₆ to the framework of ZVM. The energy of the transition state and the activation energy (ΔE_{t1}) was 46.8 kJ/mol. H2 of C₂H₅ then transferred to the framework, forming the product of C₂H₄ coordinating with Zn at a distance of 2.357 Å (Fig. 8J). The system energy of the product was 16.2 kJ/mol. The transition state (TS2) revealed that Zn interacted with C₂H₅. H2 of C₂H₅ interacted with C2 and Zn at distances of 1.375 Å and 2.511 Å (Fig. 8I). The energy of TS2 was 107.4 kJ/mol, with ΔE_{t2} of 103.7 kJ/mol (Fig. 8E).

In the case of VM, the reaction also occurred in the heptagonal channel. The intermediate of C₂H₅ also formed. Different from the case of ZVM, C1 of the intermediate interacted with O1 of VM at a distance of C1-O1 of 1.468 Å, with a system energy of 32.7 kJ/mol (Fig. 8E). The transition state (TS1') showed that H1 transferred with a distance of H1-C1 of 2.568 Å (Fig. 8E,K,L). The energy of TS1' for VM was 171.2 kJ/mol, with $\Delta E_{t1}'$ of 171.2 kJ/mol, which was higher than the energy of ΔE_{t1} for ZVM (46.8 kJ/mol) (Fig. 8E). Then, H2 migrated to O2 of the framework, forming the product of C₂H₄ with an energy of 97.1 kJ/mol (Fig. 8E,M,N,O). TS2' of VM was optimized, showing an energy of 170.9 kJ/mol with $\Delta E_{t2}'$ of 138.3 kJ/mol, also higher than the case of ZVM ($\Delta E_{t2}=103.7$ kJ/mol) (Fig. 8E).

Thus, Zn incorporation decreased the system energy of the

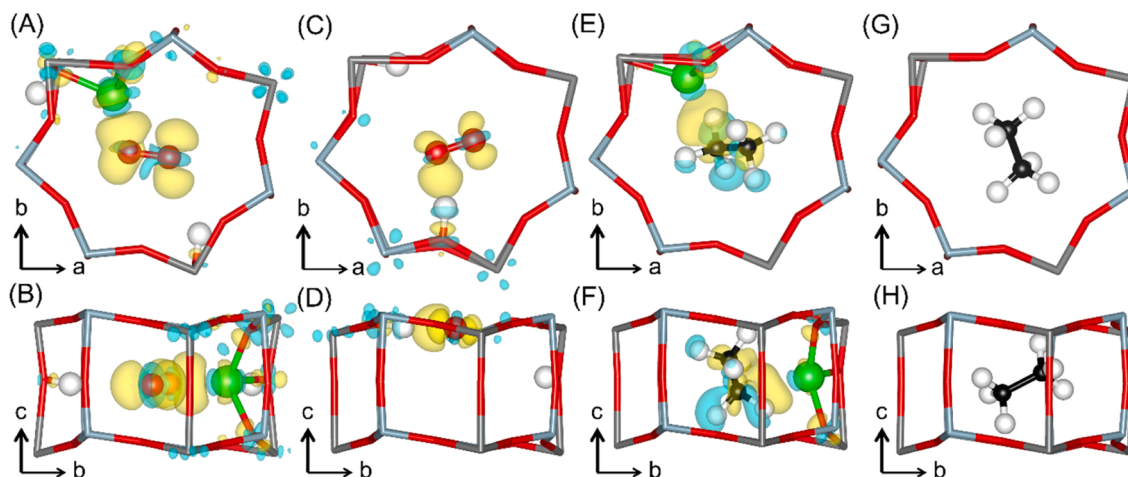


Fig. 9. The CDD images of O₂ adsorbed in the heptagonal channel of (A) and (B) ZVM, (C) and (D) VM, the CDD images of C₂H₆ adsorbed in the heptagonal channel of (E) and (F) ZVM, (G) and (H) VM. The yellow and blue isosurfaces indicating the charge gain and depletion, (isosurfaces=0.002), Mo (blue), V (gray), O (red), Zn (green), C (black), H (white).

intermediates as well as the transition state by the close interaction of Zn with C₂H₅, which was the reason that the activity of **ZVM** was higher than that of **VM**.

To further confirm the C₂H₆ ODH over the catalysts based on simulation, the reaction kinetic was investigated. First of all, factors related to transport limitations were explored by varying the total flow rate and granularity. The reaction performance remained unchanged, indicating that the transport limitations did not affect the reaction (Fig. S29). Both catalysts exhibited a similar dependence of partial pressure of C₂H₆ (0.5 for **VM** and 0.7 for **ZVM**) regarding the reaction rate (Fig. S2), while **VM** displayed a higher dependency on the partial pressure of O₂ (0.4) compared to **ZVM** (0.2). The experimental activation energy was calculated based on Arrhenius equation. The result showed that the experimental activation energy of **ZVM** was 92 kJ/mol, which was lower than that of **VM** (142 kJ/mol). This trend was consistent with the DFT calculation, indicating the reasonableness of simulation.

Recovery of the catalyst and the formation of water were simulated (Fig. S30). There were majorly two routes for water formation. In route 1, water was formed by dehydration of a lattice oxygen with two H from C₂H₆, and O₂ compensated for the lattice oxygen vacancy (O_v). The other route indicated that the adsorbed O₂ reacted with H, forming water directly. EPR analysis of **ZVM-E300** confirmed the existence of O_v, demonstrating that route 1 might be the preferred pathway for dehydration (Fig. S21A).

Total oxidation of C₂H₆ ODH was investigated by the oxidation of C₂H₄. For **ZVM**, C₂H₄ conversion obviously increased when the temperature was over 340 °C, indicating that total oxidation majorly occurred above 340 °C. **ZVM** exhibited a higher temperature for total oxidation compared to **VM** (280 °C), suggesting that Zn might suppress total oxidation and increase C₂H₄ selectivity at lower temperatures (Fig. S31). The mechanism of total oxidation was simulated using DFT calculation. Both MvK and Langmuir-Hinshelwood (LH) mechanisms were tested (Fig. S32). MvK mechanism indicated that the energy of dehydrogenation product (C₂H₄) was lower than the energy of the total oxidation intermediate (CH₃CHO) [76,77]. In contrast, LH mechanism showed a different result from MvK mechanism, with the energy of the total oxidation intermediate being lower. At lower temperatures, C₂H₄ was the major product, but as the temperature increased, CO₂ selectivity increased. Therefore, C₂H₆ ODH majorly followed MvK mechanism at lower temperatures, while total oxidation followed LH mechanism at higher temperatures.

4. Conclusion

In summary, the Zn incorporated vanadomolybdate was synthesized for C₂H₆ ODH. The incorporation of Zn did not change the structure of the material. Zn was found to be located in the heptagonal channel of the material, as determined by the powder XRD and the DFT calculation. Zn incorporation activated both O₂ and C₂H₆, causing oxidation of V in the material and C₂H₆ ODH at a lower temperature. The catalytic activity of **ZVM** for C₂H₆ ODH (45 % of C₂H₄ yield) was higher than that of **VM** without Zn (26 % of C₂H₄ yield) at the same temperature, highlighting the essential role of Zn in achieving high catalytic activity. The reaction mechanism study revealed that Zn played a key role in coordinating the intermediate of C₂H₅ and stabilizing it, as well as stabilizing the transition state of the reaction catalyst by the material.

CRediT authorship contribution statement

Conceptualization: **Zhenxin Zhang**. Funding acquisition: **Zhenxin Zhang, Qianqian Zhu, Yanshuo Li**. Investigation: **Bolun Yu, Denan Li, Shufan Yao, Lifeng Zhang**. Supervision: **Zhenxin Zhang, Qianqian Zhu, Yanshuo Li**. Writing – original draft: **Bolun Yu, Zhenxin Zhang**. Writing – review & editing: **Qianqian Zhu, Zhenxin Zhang**.

Declaration of Competing Interest

The authors declare that they have no known competing financial interests or personal relationships that could have appeared to influence the work reported in this paper.

Data availability

Data will be made available on request.

Acknowledgments

This work is supported by National Key Technologies R&D Program (Grant No. 2022YFE0108000), the National Natural Science Foundation of China (Grant No. 22075153 and 22006077), Ningbo Young Technological Innovation Leaders Program (Grant No. 2023QL048), and Leading Innovation and Entrepreneurship Team in Zhejiang Province.

Appendix A. Supporting information

Supplementary data associated with this article can be found in the online version at doi:10.1016/j.apcatb.2023.123463.

References

- [1] C.A. Gärtner, A.C. vanVeen, J.A. Lercher, Oxidative dehydrogenation of ethane: common principles and mechanistic aspects, *ChemCatChem* 5 (2013) 3196–3217.
- [2] N. Raja, G.M. Monsalve-Bravo, Y.V. Kaneti, J. Mensah, K. Wilson, A.F. Lee, M. Konarova, Thermogravimetric kinetic analysis of catalytic and non-catalytic pyrolysis of simulated municipal solid waste, *Chem. Eng. J.* 470 (2023), 144046.
- [3] W. Gong, T. Wang, L. Wang, X. He, Y. Yao, S.T. Tjeng, D. Ding, M. Fan, High-performance of CrO_x/HZSM-5 catalyst on non-oxidative dehydrogenation of C₂H₆ to C₂H₄: effect of supporting materials and associated mechanism, *Fuel Process. Technol.* 233 (2022), 107294.
- [4] O.O. James, S. Mandal, N. Alele, B. Chowdhury, S. Maity, Lower alkanes dehydrogenation: strategies and reaction routes to corresponding alkenes, *Fuel Process. Technol.* 149 (2016) 239–255.
- [5] M.H.M. Ahmed, N. Batalha, M.R. Karim, I.A. Alnaser, Y. Yamauchi, Y.V. Kaneti, M. Konarova, Design of trifunctional catalysts for promoting sequential condensation, deoxygenation, and aromatization of pyrolyzed mixed waste, *J. Mater. Chem. A* 11 (2023) 14404–14415.
- [6] P. Novotny, S. Yusuf, F. Li, H.H. Lamb, MoO₃/Al₂O₃ catalysts for chemical-looping oxidative dehydrogenation of ethane, *J. Chem. Phys.* 152 (2020), 044713.
- [7] J. Chen, Z. Sun, V. Balakotaiah, P. Bollini, A global kinetic model for the oxidative dehydrogenation of ethane over mixed metal oxide catalysts at supra-ambient pressures, *Chem. Eng. J.* 445 (2022), 136605.
- [8] S. Yacob, M. Caulfield, R.B. Larson, E. Gomez, R.J. Meyer, The interplay between process conceptualization and experimental research-accelerating and guiding catalysis to process breakthroughs, *ACS Catal.* 12 (2022) 10621–10628.
- [9] M. Baerns, O. Buyevskaya, Simple chemical processes based on low molecular-mass alkanes as chemical feedstocks, *Catal. Today* 45 (1998) 13–22.
- [10] D. Vitry, Y. Morikawa, J.L. Dubois, W. Ueda, Mo-V-Te-(Nb)-O mixed metal oxides prepared by hydrothermal synthesis for catalytic selective oxidations of propane and propene to acrylic acid, *Appl. Catal. A Gen.* 251 (2003) 411–424.
- [11] A. Alamdari, R. Karimzadeh, S. Abbasizadeh, Present state of the art of and outlook on oxidative dehydrogenation of ethane: catalysts and mechanisms, *Rev. Chem. Eng.* 37 (2021) 481–532.
- [12] G. Luongo, F. Donat, A.H. Bork, E. Willinger, A. Landuyt, C.R. Müller, Highly selective oxidative dehydrogenation of ethane to ethylene via chemical looping with oxygen uncoupling through structural engineering of the oxygen carrier, *Adv. Energy Mater.* 12 (2022), 2200405.
- [13] S. Najari, S. Saeidi, P. Concepcion, D.D. Dionysiou, S.K. Bhargava, A.F. Lee, K. Wilson, Oxidative dehydrogenation of ethane: catalytic and mechanistic aspects and future trends, *Chem. Soc. Rev.* 50 (2021) 4564–4605.
- [14] F. Donsi, S. Cimino, R. Pirone, G. Russo, D. Sanfilippo, Crossing the breakthrough line of ethylene production by short contact time catalytic partial oxidation, *Catal. Today* 106 (2005) 72–76.
- [15] S. Cimino, F. Donsi, G. Russo, D. Sanfilippo, Olefins production by catalytic partial oxidation of ethane and propane over Pt/LaMnO₃ catalyst, *Catal. Today* 157 (2010) 310–314.
- [16] F. Cavani, F. Trifiro, Selective oxidation of light alkanes: interaction between the catalyst and the gas phase on different classes of catalytic materials, *Catal. Today* 51 (1999) 561–580.
- [17] V.R. Choudhary, S.A.R. Mulla, V.H. Rane, Coupling of exothermic and endothermic reactions in oxidative conversion of ethane to ethylene over alkaline earth promoted La₂O₃ catalysts in presence of limited O₂, *Appl. Energy* 66 (2000) 51–62.

- [18] L. Liu, H. Li, H. Zhou, S. Chu, L. Liu, Z. Feng, X. Qin, J. Qi, J. Hou, Q. Wu, H. Li, X. Liu, L. Chen, J. Xiao, L. Wang, F.-S. Xiao, Rivet of cobalt in siliceous zeolite for catalytic ethane dehydrogenation, *Chem* 9 (2023) 637–649.
- [19] Z. Geng, Y. Zhang, H. Deng, S. Wang, H. Dong, Multiscale modeling and simulation on oxidative dehydrogenation of ethane to ethylene, *Chem. Eng. Res. Des.* 195 (2023) 235–246.
- [20] H.X. Dai, C.F. Ng, C.T. Au, $\text{YBa}_2\text{Cu}_3\text{O}_{7-\delta}\text{X}_\alpha$ ($\text{X}=\text{F}$ and Cl): highly active and durable catalysts for the selective oxidation of ethane to ethene, *J. Catal.* 193 (2000) 65–79.
- [21] B. Tope, Y. Zhu, J.A. Lercher, Oxidative dehydrogenation of ethane over $\text{Dy}_2\text{O}_3/\text{MgO}$ supported LiCl containing eutectic chloride catalysts, *Catal. Today* 123 (2007) 113–121.
- [22] P. Botella, A. Dejoz, M.C. Abello, M.I. Vázquez, L. Arrúa, J.M. López, Nieto, selective oxidation of ethane: developing an orthorhombic phase in $\text{Mo}-\text{V}-\text{X}$ ($\text{X}=\text{Nb}, \text{Sb}, \text{Te}$) mixed oxides, *Catal. Today* 142 (2009) 272–277.
- [23] F. Cavani, J.H. Teles, Sustainability in catalytic oxidation: an alternative approach or a structural evolution? *ChemSusChem* 2 (2009) 508–534.
- [24] Z. Skoufa, E. Heracleous, A.A. Lemonidou, Unraveling the contribution of structural phases in $\text{Ni}-\text{Nb}-\text{O}$ mixed oxides in ethane oxidative dehydrogenation, *Catal. Today* 192 (2012) 169–176.
- [25] J.F. Durán-Pérez, J.G. Rivera de la Cruz, C.O. Castillo-Araiza, Elucidating selective and total oxidation elementary reactions over a Ni-based catalyst for sustainable ethylene production via oxidative dehydrogenation of ethane: microkinetic analysis, *Chem. Eng. J.* 470 (2023), 143939.
- [26] C. Wang, M. Tian, Y. Han, T. Tong, N. Wang, L. Li, J. Lin, X. Wang, Dual Ni active sites mediated by In to separate ethane activation and oxidation for enhanced ethene production via chemical looping scheme, *Appl. Catal. B Environ.* 325 (2023), 122334.
- [27] Y. Briki, M. Kacimi, M. Ziyad, F. Bozon-Verduraz, Titania-supported cobalt and cobalt-phosphorus catalysts: characterization and performances in ethane oxidative dehydrogenation, *J. Catal.* 202 (2001) 118–128.
- [28] G. d N. Franceschini, P. Concepción, M. Schwaab, M. do Carmo Rangel, J. Martínez-Triguero, J.M. López, Nieto, Spectroscopic insights into the role of CO_2 on the nature of Cr species in a $\text{CrO}_x/\text{Al}_2\text{O}_3$ catalysts during ethane dehydrogenation with CO_2 , *Appl. Catal. A Gen.* 661 (2023), 119260.
- [29] M.A. Artsusheuski, R. Verel, J.A. van Bokhoven, V.L. Sushkevich, Selective oxidative dehydrogenation of ethane and propane over copper-containing mordenite: insights into reaction mechanism and product protection, *Angew. Chem. Int. Ed.* 12 (2023) 09180.
- [30] Y. Dai, X. Gao, Q. Wang, X. Wan, C. Zhou, Y. Yang, Recent progress in heterogeneous metal and metal oxide catalysts for direct dehydrogenation of ethane and propane, *Chem. Soc. Rev.* 50 (2021) 5590–5630.
- [31] A. Massó Ramírez, F. Ivars-Barceló, J.M. López Nieto, Optimizing reflux synthesis method of Mo-V-Te-Nb mixed oxide catalysts for light alkane selective oxidation, *Catal. Today* 356 (2020) 322–329.
- [32] P. Botella, E. García-González, J.M. López Nieto, J.M. González-Calbet, MoVTeNbO multifunctional catalysts: correlation between constituent crystalline phases and catalytic performance, *Solid. State Sci.* 7 (2005) 507–519.
- [33] G. Che-Galicia, R. Quintana-Solórzano, R.S. Ruiz-Martínez, J.S. Valente, C. O. Castillo-Araiza, Kinetic modeling of the oxidative dehydrogenation of ethane to ethylene over a MoVTeNbO catalytic system, *Chem. Eng. J.* 252 (2014) 75–88.
- [34] B. Deniau, J.M.M. Millet, S. Loridan, N. Christin, J.L. Dubois, Effect of several cationic substitutions in the M1 active phase of the MoVTeNbO catalysts used for the oxidation of propane to acrylic acid, *J. Catal.* 260 (2008) 30–36.
- [35] Y. Chen, B. Yan, Y. Cheng, State-of-the-art review of oxidative dehydrogenation of ethane to ethylene over MoVNbTeO_x catalysts, *Catalysts* 13 (2023) 204.
- [36] S. Ishikawa, W. Ueda, Microporous crystalline Mo-V mixed oxides for selective oxidations, *Catal. Sci. Technol.* 6 (2016) 617–629.
- [37] F. Ivars-Barceló, B. Solsona, E. Asedegbeaga-Nieto, J.M. López Nieto, Enhancement of ethylene production by alkali metal doping of MoVSb mixed oxide catalyst for ethane oxidative dehydrogenation, *Appl. Catal. A Gen.* 660 (2023), 119200.
- [38] J. Wang, Q. Zhu, Z. Zhang, M. Sadakane, Y. Li, W. Ueda, Zeolitic octahedral metal oxides with ultra-small micropores for C_2 hydrocarbon separation, *Angew. Chem. Int. Ed.* 60 (2021) 18328–18334.
- [39] B. Ma, D. Li, Q. Zhu, Y. Li, W. Ueda, Z. Zhang, A zeolitic octahedral metal oxide with ultra-microporosity for inverse $\text{CO}_2/\text{C}_2\text{H}_2$ separation at high temperature and humidity, *Angew. Chem. Int. Ed.* 61 (2022), e202209121.
- [40] T. Konya, T. Katou, T. Murayama, S. Ishikawa, M. Sadakane, D. Buttrey, W. Ueda, An orthorhombic Mo_3VO_x catalyst most active for oxidative dehydrogenation of ethane among related complex metal oxides, *Catal. Sci. Technol.* 3 (2013) 380–387.
- [41] S. Ishikawa, Y. Yamada, C. Qiu, Y. Kawahara, N. Hiyoshi, A. Yoshida, W. Ueda, Synthesis of a crystalline orthorhombic Mo-V-Cu oxide for selective oxidation of acrolein, *Chem. Mater.* 31 (2019) 1408–1417.
- [42] Y.S. Yun, M. Lee, J. Sung, D. Yun, T.Y. Kim, H. Park, K.R. Lee, C.K. Song, Y. Kim, J. Lee, Y.-J. Seo, I.K. Song, J. Yi, Promoting effect of cerium on MoVTeNb mixed oxide catalyst for oxidative dehydrogenation of ethane to ethylene, *Appl. Catal. B Environ.* 237 (2018) 554–562.
- [43] M. Sadakane, K. Kodato, T. Kuranishi, Y. Nodasaka, K. Sugawara, N. Sakaguchi, T. Nagai, Y. Matsui, W. Ueda, Molybdenum-vanadium-based molecular sieves with microchannels of seven-membered rings of corner-sharing metal oxide octahedra, *Angew. Chem. Int. Ed.* 47 (2008) 2493–2496.
- [44] R.J. Madon, M. Boudar, Experimental criterion for the absence of artifacts in the measurement of rates of heterogeneous catalytic reaction, *Ind. Eng. Chem. Fundam.* 21 (1982) 438–447.
- [45] R.M. Koros, E.J. Nowak, A diagnostic test of the kinetic regime in a packed bed reactor, *Chem. Eng. Sci.* 22 (1967) 470.
- [46] G. Kresse, Ab-initio molecular-dynamics for liquid-metals, *J. Non-Cryst. Solids* 193 (1995) 222–229.
- [47] G. Kresse, J. Hafner, Ab initio molecular dynamics for liquid metals, *Phys. Rev. B Condens. Matter* 47 (1993) 558–561.
- [48] J.P. Perdew, K. Burke, M. Ernzerhof, Generalized gradient approximation made simple, *Phys. Rev. Lett.* 77 (1996) 3865–3868.
- [49] P.E. Blöchl, Projector augmented-wave method, *Phys. Rev. B* 50 (1994) 17953.
- [50] S. Grimme, J. Antony, S. Ehrlich, H. Krieg, A consistent and accurate ab initio parametrization of density functional dispersion correction (DFT-D) for the 94 elements H-Pu, *J. Chem. Phys.* 132 (2010), 154104.
- [51] C.-R. Hu, Heat-current operator and transport entropy of vortices in type-II superconductors, *Phys. Rev. B* 13 (1976) 4780–4783.
- [52] V. Wang, N. Xu, J.-C. Liu, G. Tang, W.-T. Geng, VASPKIT: a user-friendly interface facilitating high-throughput computing and analysis using VASP code, *Comput. Phys. Commun.* 267 (2021), 108033.
- [53] S. Ishikawa, X. Yi, T. Murayama, W. Ueda, Heptagonal channel micropore of orthorhombic Mo_3VO_x as catalysis field for the selective oxidation of ethane, *Appl. Catal. A Gen.* 474 (2014) 14–17.
- [54] L. Annamalai, Y. Liu, S. Ezenwa, Y. Dang, S.L. Suib, P. Deshlahra, Influence of tight confinement on selective oxidative dehydrogenation of ethane on MoVTeNb mixed oxides, *ACS Catal.* 8 (2018) 7051–7067.
- [55] T.A. Halgren, W.N. Lipscomb, The synchronous-transit method for determining reaction pathways and locating molecular transition states, *Chem. Phys. Lett.* 49 (1977) 225–232.
- [56] G. Henkelman, B.P. Uberuaga, H. Jonsson, A climbing image nudged elastic band method for finding saddle points and minimum energy paths, *J. Chem. Phys.* 113 (2000) 9901–9904.
- [57] G. Henkelman, H. Jonsson, Improved tangent estimate in the nudged elastic band method for finding minimum energy paths and saddle points, *J. Chem. Phys.* 113 (2000) 9978–9985.
- [58] B. Liu, L. Yan, H. Zhao, J. Yang, J. Zhao, H. Song, L. Chou, Role of cerium dopants in MoVNbO multi-metal oxide catalysts for selective oxidation of ethane, *J. Rare. Earth* 40 (2022) 753–762.
- [59] A. Trunschke, J. Noack, S. Trojanov, F. Girgsdies, T. Lunkenbein, V. Pfeifer, M. Hävecker, P. Kube, C. Sprung, F. Rosowski, R. Schlögl, The impact of the bulk structure on surface dynamics of complex Mo-V-based oxide catalysts, *ACS Catal.* 7 (2017) 3061–3071.
- [60] Y. Liu, L. Annamalai, P. Deshlahra, Effects of lattice O atom coordination and pore confinement on selectivity limitations for ethane oxidative dehydrogenation catalyzed by vanadium-oxo species, *J. Phys. Chem. C* 123 (2019) 28168–28191.
- [61] M.-J. Cheng, W.A. Goddard, In silico design of highly selective Mo-V-Te-Nb-O mixed metal oxide catalysts for ammonoxidation and oxidative dehydrogenation of propane and ethane, *J. Am. Chem. Soc.* 137 (2015) 13224–13227.
- [62] M. Hävecker, S. Wrabetz, J. Kröhnert, L.-I. Csepei, R.N. d'Alnoncourt, Y. V. Kolen'ko, F. Girgsdies, R. Schlögl, A. Trunschke, Surface chemistry of phase-pure M1 MoVTeNb oxide during operation in selective oxidation of propane to acrylic acid, *J. Catal.* 285 (2012) 48–60.
- [63] P. D Jr., D.J. Buttrey, R.K. Grasselli, C.G. Lugmair, A.F. Volpe, B.H. Toby, T. Vogtd, Structural characterization of the orthorhombic phase M1 in MoVNbTeO propane ammonoxidation catalyst, *Top. Catal.* 23 (2003) 1–4.
- [64] Y. Zhu, P.V. Sushko, D. Melzer, E. Jensen, L. Kovarik, C. Ophus, M. Sanchez-Sánchez, J.A. Lercher, N.D. Browning, Formation of oxygen radical sites on MoVNbTeO_x by cooperative electron redistribution, *J. Am. Chem. Soc.* 139 (2017) 12342–12345.
- [65] E. Heracleous, A.A. Lemonidou, J.A. Lercher, Mechanistic features of the ethane oxidative dehydrogenation by *in situ* FTIR spectroscopy over a $\text{MoO}_3/\text{Al}_2\text{O}_3$ catalyst, *Appl. Catal. A Gen.* 264 (2004) 73–80.
- [66] R. Zhang, H. Wang, S. Tang, C. Liu, F. Dong, H. Yue, B. Liang, Photocatalytic oxidative dehydrogenation of ethane using CO_2 as a soft oxidant over Pd/TiO_2 catalysts to C_2H_4 and syngas, *ACS Catal.* 8 (2018) 9280–9286.
- [67] X. Li, Y. Zhou, B. Qiao, X. Pan, C. Wang, L. Cao, L. Li, J. Lin, X. Wang, Enhanced stability of $\text{Pt}/\text{Al}_2\text{O}_3$ modified by Zn promoter for catalytic dehydrogenation of ethane, *J. Energy Chem.* 51 (2020) 14–20.
- [68] B. Yang, X. Cheng, Y. Zhang, W. Li, J. Wang, Z. Tian, E. Du, H. Guo, Staged assessment for the involving mechanism of humic acid on enhancing water decontamination using $\text{H}_2\text{O}_2\text{-Fe(III)}$ process, *J. Hazard. Mater.* 407 (2021), 124853.
- [69] L. Wang, X. Lan, W. Peng, Z. Wang, Uncertainty and misinterpretation over identification, quantification and transformation of reactive species generated in catalytic oxidation processes: a review, *J. Hazard. Mater.* 408 (2021), 124436.
- [70] M. Wu, Y. Zhang, Y. Yi, B. Zhou, P. Sun, X. Dong, Regulation of friction pair to promote conversion of mechanical energy to chemical energy on Bi_2WO_6 and realization of enhanced tribocatalytic activity to degrade different pollutants, *J. Hazard. Mater.* 459 (2023), 132147.
- [71] C. Decroos, Y. Li, G. Bertho, Y. Frapart, D. Mansuy, J.-L. Boucher, Oxidation of tris-(*p*-carboxyltetrahydralyl)methyl radical EPR probes: evidence for their oxidative decarboxylation and molecular origin of their specific ability to react with O_2^- , *Chem. Commun.* 11 (2009) 1416–1418.
- [72] J.J. Ternero-Hidalgo, M. Daturi, G. Clet, P. Bazin, M.A. Bañares, R. Portela, M. O. Guerrero-Pérez, J. Rodríguez-Mirasol, T. Cordero, A simultaneous operando FTIR & Raman study of propane ODH mechanism over V-Zr-O catalysts, *Catal. Today* 387 (2022) 197–206.
- [73] R. Singh, M. Banares, G. Deo, Effect of phosphorous modifier on $\text{V}_2\text{O}_5/\text{TiO}_2$ catalyst: ODH of propane, *J. Catal.* 233 (2005) 388–398.

- [74] E. Heracleous, A. Lemonidou, Ni–Nb–O mixed oxides as highly active and selective catalysts for ethene production via ethane oxidative dehydrogenation. Part II: mechanistic aspects and kinetic modeling, *J. Catal.* 237 (2006) 175–189.
- [75] B. Beck, M. Harth, N.G. Hamilton, C. Carrero, J.J. Uhlrich, A. Trunschke, S. Shaikhutdinov, H. Schubert, H.-J. Freund, R. Schlögl, J. Sauer, R. Schomäcker, Partial oxidation of ethanol on vanadia catalysts on supporting oxides with different redox properties compared to propane, *J. Catal.* 296 (2012) 120–131.
- [76] D. Guoliang, L. Zhenhua, W. Wenning, L. Jing, F. Kangnian, Periodic DFT study of the deep oxidation in the oxidative dehydrogenation of ethane over V₂O₅(001), *Chin. J. Catal.* 34 (2013) 906–910.
- [77] H. Fu, Z.-P. Liu, Z.-H. Li, W.-N. Wang, K.-N. Fan, Periodic density functional theory study of propane oxidative dehydrogenation over V₂O₅(001) surface, *J. Am. Chem. Soc.* 28 (2006) 11114–11123.